AIAA SciTech Forum
6-10 January 2025, Orlando, FL
AIAA SCITECH 2025 Forum

10.2514/6.2025-2503

Numerical investigation of gas turbine combustor cooling performance with Bézier effusion holes

Nicholas C. Lopes[*], Mark A. Ricklick[†], Sandra K.S. Boetcher [‡]
Embry-Riddle Aeronautical University, Daytona Beach, FL USA 32114

Bertram Janus[§], Thomas Behrendt[¶], Ralf Becker [‖]
Deutsches Zentrum für Luft- und Raumfahrt (DLR), Linder Höhe, Köln DEU 51147

A novel gas turbine combustor effusion hole concept was simulated under realistic fuel-lean operating conditions in the present work. The hole's bore was defined using a quadratic Bézier curve, enabling efficient cooling air injection over the liner. Modifications to the hole's inlet and width expansion were made to observe their effect on cooling performance. Results show that the addition of an inlet fillet increased velocity in the hole and improved flow attachment, but had marginal impact on liner temperature. A higher width expansion yielded greater cooling effectiveness and a more uniform surface heat flux distribution. A narrower injection hole generally increased streamwise jet momentum and resulted in lift-off and localized hot spots due to counter-rotating vortices. Complex effusion holes, such as those presented here, will be facilitated by advances in additive manufacturing and serve to improve the thermal efficiency of gas turbines.

I. Nomenclature

a = semi-major axis (m)
B = Bezier curve
b = semi-minor axis (m)
C = control point
c = ellipse center point (m)
D = hole diameter (m)
d = fillet diameter of the hole inlet (m)
E_c = expansion coefficient
E_r = expansion ratio
e = ellipse
G = mass flux (kg/(m^2 s))
h = heat transfer coefficient (W/(m^2 K))
L = grid pattern length
LES = large eddy simulation
Nu = Nusselt number
P = pressure (Pa)
q = wall heat flux (W/m^2)
RANS = Reynolds-averaged Navier-Stokes
$\hat{r}$ = unit vector
T = temperature (K)
t = parametric variable
u , v , w = velocity components (m/s)

---

[*] PhD Student, Department of Mechanical Engineering
[†] Associate Professor, Department of Aerospace Engineering
[‡] Professor, Department of Mechanical Engineering
[§] Institute of Propulsion Technology
[¶] Institute of Propulsion Technology
[‖] Institute of Propulsion Technology

x , y , z = cartesian coordinates (m)
y^+ = nondimensional distance from wall to first cell centroid
y^* = nondimensional distance from wall into the flow

Greek Symbols

δ = expansion curve
η = cooling effectiveness
λ = thermal conductivity (W/(m K))
ϕ = angle around the ellipse

Subscripts

$cold$ = cold-side
hot = hot-side
in = inlet
out = outlet
pt = monitor point
$span$ = spanwise
w = wall

II. Introduction

There are continuing economic and environmental demands for the development of more fuel-efficient aircraft engines [1]. This is accomplished through higher thrust and core efficiencies. The thermal efficiency of the core is enhanced by increasing the overall pressure ratio and turbine inlet temperature. While maximizing these design parameters generally serve to decrease CO and soot emissions, they have an adverse effect on NO_x production [2].

To simultaneously improve efficiency and mitigate emission issues, a rich-quench-lean combustor design is often implemented. This combustion process starts with a fuel-rich mixture and is subsequently quenched by cooling air before finishing in a fuel-lean state, ensuring complete combustion. Rich-quench-lean typically provides enhanced combustion stability and power density, but suffers from increased system complexity and limited NO_x reduction potential [3].

Alternative emission reduction techniques, such as fuel-lean combustion, have gained recent popularity. In this process, the air-fuel ratio is higher than the stoichiometric ratio during the entire combustion process. The excess oxygen induces a more homogenized mixture and lower flame temperature. This serves to reduce NO_x formation through more complete combustion as well as improve component life through reduced thermal loading on the liner [4].

The cooling requirements and constraints for the liner indeed depend on the specific combustor configuration. For a fuel-lean cooling design, the primary challenge is the overall reduction in available cooling air. This necessitates the development of new and predictable techniques which employ principles such as effusion cooling [5].

Effusion cooling utilizes an evenly distributed matrix of small holes—diameters typically on the order of 0.1–1 mm—on the combustor liner, allowing cooling air from the surrounding plenum to uniformly cover the inner (hot-side) surface. Historically, effusion design parameters—the quantity, shape, angle, and size of the holes—have been hindered by manufacturing limitations. However, recent additive manufacturing techniques enable the development of sophisticated hole geometries capable of meeting both the reduced mass flow restrictions and cooling requirements of fuel-lean combustors.

A novel fuel-lean combustor effusion hole—whose contour was inspired by a quadratic Bézier curve—is introduced and its cooling performance is numerically investigated in this work. The simulated liner was exposed to realistic bulk conditions typical of a modern fuel-lean combustor and plenum. The implemented numerical schemes were validated against experimental and other (validated) numerical results [6–9]. A preliminary optimization of the hole geometry is also provided at the specified conditions. The results presented here will serve as the basis for a future experimental campaign carried out at the Deutsches Zentrum für Luft- und Raumfahrt (DLR) High Pressure Combustor Cooling Test Rig, enabled by the advanced additive manufacturing capabilities at their facilities.

III. Methodology

A. Physical model and boundary conditions

The geometry and conditions studied here (Fig. 1) were inspired by a series of experiments conducted at the DLR High Pressure Combustor Cooling Test Rig by Behrendt and Hassa [6]. A periodic slice of an Inconel 718 combustor liner separates two parallel flow channels. The hot and cold gas paths emulate specified combustor and cooling plenum conditions, respectively. The liner is 1.5 mm thick and consists of a grid of 24 effusion holes staggered among three spanwise rows which, through an imposed pressure gradient, supply air from the plenum to the hot-side wall.

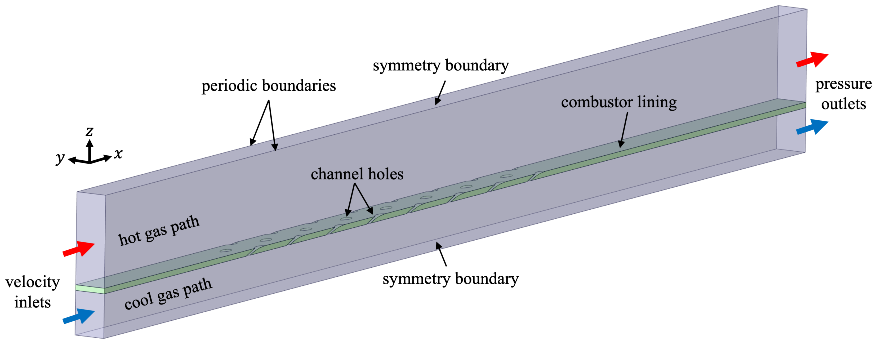

Fig. 1 Model and boundary conditions.

Uniform velocity profiles were prescribed at the inlets. The combustor and coolant pressures were defined at the respective outlets. The hot- and cold-side outlets were situated relatively far from the grid to reduce any backflow effects. The height of the hot- and cold-side domains were set such that the boundaries would not influence the flow physics near the liner while minimizing computational resources. Thus, either wall or symmetry (zero-gradient) boundaries could be used with negligible consequence; symmetry boundaries were selected. Periodic boundaries were assigned in the spanwise direction. The solid and fluid domains were coupled at their interface for conjugate heat transfer analysis.

Fig. 2 details the configuration of the liner grid. The spanwise (periodic) boundaries were taken at the centerlines of the first and third hole rows. The staggered row pattern was repeated eight times in the streamwise direction to ensure full flow and thermal development. The holes do not have a streamwise angle; they are oriented symmetrically about the x-axis.

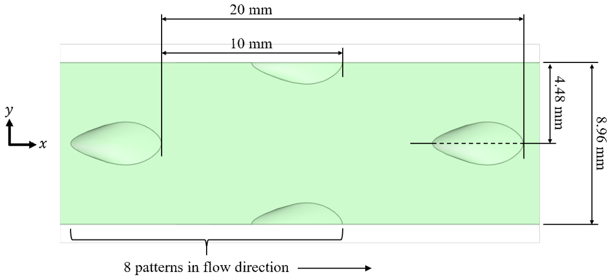

Fig. 2 Grid configuration.

The conditions TC2 from Behrendt and Hassa [6] were imposed at the boundaries. The hot- and cold-side inlet temperature, outlet pressure, and inlet velocities are provided in Table 1. The cold-side inlet velocity, while not given explicitly, was calculated using the cooling area and mass flow of the test rig in [6]. The physical properties for Inconel 718 were taken from Agazhanov et al. [10] at 1,100 K—the intermediate temperature between the hot and cold inlets.

B. Baseline hole geometry

Fig. 3 illustrates a side and top view of the baseline hole geometry. Unlike combustor effusion holes found in the literature, which often feature a cylindrical hole with a linear bore angle, the unique hole shape introduced here features

Table 1 Operating conditions for TC2 in Behrendt and Hassa [6].

Parameter	Hot path	Cold path
T_{in} (K)	1750	480
P_{out} (bar)	5	5.085 ($\Delta P = 1.7\%$)
u_{in} (m/s)	30	64

a complex, curved bore in both the vertical and streamwise directions. The hole was extracted from a mathematically defined solid.

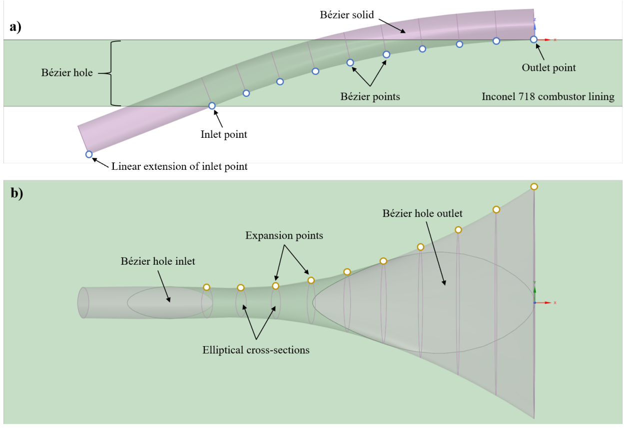

Fig. 3 Bézier solid and the extracted hole: a) Bézier points define vertical profile and b) expansion points define spanwise profile.

The vertical profile of the solid is defined by a Bézier curve—a smooth and continuous parametric function often used for approximating complex curves. The *quadratic* Bézier curve was implemented, and is given as

$$B(t) = (1-t)^2 C_{out} + 2(1-t)tC_{var} + t^2 C_{in} \tag{1}$$

where $B(t)$ is the Bézier curve and is a function of the parameter t, whose range is $0 \leq t \leq 1$. The resolution of the curve is determined by t. For the present application, the shape of the solid was sufficiently resolved with 10 equally spaced values of t between 0 and 1.

The shape of a quadratic Bézier curve is defined by a set of three control points. The control points and the resulting Bézier curve used here are shown in Fig. 4. The leftmost and rightmost control points—corresponding to points at the hole inlet (bottom surface) and outlet (top surface) in Fig. 3(a)—are denoted C_{in} and C_{out}, respectively.

The locations of C_{in} and C_{out} are given in Table 2. Also provided are the inlet and outlet bore angles of the Bézier hole with respect to the $+z$-axis (moving in the clockwise direction). The locations and bore angles of these points were selected with the intention of gradually and efficiently guiding the cooling flow to the top (hot) surface. The bore angles are illustrated in Fig. 4 as the lines protruding from the inlet and outlet points; they intersect at a third point, called here the variable point C_{var}. This intersection point was used as the third control point to define the Bézier curve. Its location is given in Table 2.

The solid itself has a constant height (Fig. 3(a)) of $D = 7$ mm and a given expansion in the spanwise direction (Fig. 3(b)). By inspection of Fig. 3, it is clear that the cross sections of the solid are elliptical. An ellipse was defined at each Bézier point and lies on a plane perpendicular to the Bézier curve at that location. The semi-minor (vertical) axis b of each ellipse at a given Bézier point is $b = D = 7$ mm. The expansion $\delta(t)$ of the semi-major (spanwise) axis was defined by a parametric function, also based on t, and is given as

$$\delta(t) = E_c t^2 + (E_r - 1 - E_c)t + 1 \tag{2}$$

where the same 10 values of t were again used here. The expansion ratio E_r sets the ratio between the outlet and inlet areas of the solid. For the baseline hole shown in Fig. 3, $E_r = 7.5$. The expansion coefficient E_c influences the shape of

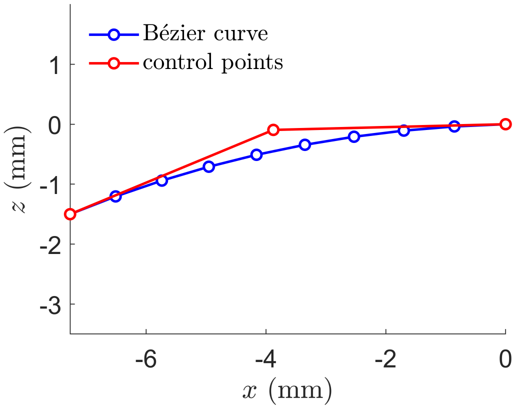

Fig. 4 Control points and resulting Bézier curve.

Table 2 Control points to define Bézier curve.

Control point	Location [x y z] (mm)	Bore angle (+z-axis) (°)
Inlet (C_{in})	[-7.27 0 -1.5]	67.5
Variable (C_{var})	[-3.88 0 -0.095]	–
Outlet (C_{out})	[0 0 0]	88.6

the spanwise expansion for a fixed expansion ratio. The length of the semi-major axis is then $a(t) = D\delta(t)$, such that a circular cross section is obtained at the inlet point (i.e. $a(0) = b = D$).

Using the semi-minor and semi-major axes at each Bézier point, the equation for the corresponding ellipse $e(\phi, t)$ is then

$$e(\phi,t) = c(t) + \frac{a(t)}{2} cos(\phi)\hat{r}_a(t) + bsin(\phi)\hat{r}_b(t) \tag{3}$$

where $c(t)$ is the center of the ellipse and $0 \leq \phi \leq 2\pi$ is the angle around the ellipse. The unit vector of the semi-major axis $\hat{r}_a(t)$ is simply in the direction of the $+y$-axis. The semi-minor axis unit vector $\hat{r}_b(t)$ is the cross-product between the semi-major axis and the unit vector tangent to the Bézier curve at a given point. Together, the semi-major and semi-minor axis unit vectors define the plane on which a given ellipse lies.

To guarantee that the solid penetrated the entire thickness of the liner, the cross section at the inlet point was linearly extended for an arbitrary length. The Bézier hole was then extracted from the liner using this final constructed solid.

C. Hole variations

The baseline hole geometry was altered to observe the effects on the flow and thermal characteristics near the hot-side wall. Fig. 5 illustrates the first two variations v1 and v2 compared to the baseline, where the trailing edge of the hole's inlet was rounded with a fillet diameter d in an attempt to mitigate potential stagnation. Three other variations, v3 - v5, are shown in Fig. 6 next to the baseline. Here, expansion ratio E_r and expansion coefficient E_c were modified. For v3 - v5, the leading edge of the hole's inlet was slightly tapered to more effectively guide the flow through the effusion hole. The relevant parameters for each variation are quantified in Table 3.

D. Numerical settings

The simulations were performed in ANSYS Fluent v23.1 using a steady-state Reynolds-averaged Navier-Stokes (RANS) approach to approximate the flow field. The energy equation was enabled for heat transfer calculations within

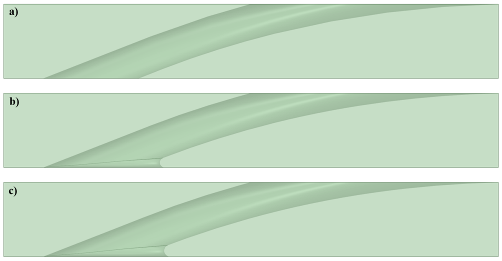

Fig. 5 Side view of a) baseline, b) v1, and c) v2 holes.

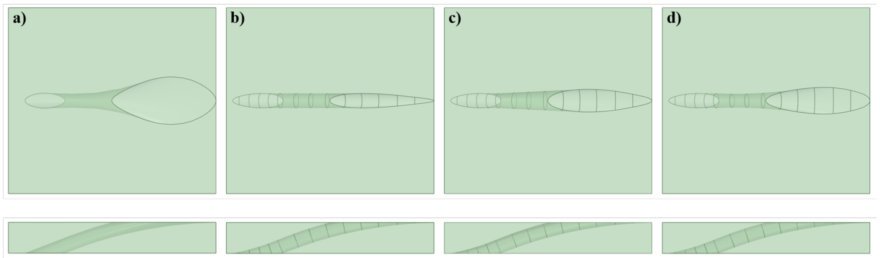

Fig. 6 Top and side view of a) baseline, b) v3, c) v4, and d) v5 holes.

Table 3 Relevant parameters for hole variation.

Hole	E_r	E_c	d (mm)
baseline	7.5	8	0
v1	7.5	8	0.1
v2	7.5	8	0.12
v3	1	0	0
v4	2	0	0
v5	3.5	3.25	0

the solid and fluid domains. Turbulence was resolved using the $k-\omega$ SST model for its balance between computational efficiency and solution accuracy for problems of this nature [11–13].

1. Mesh considerations

The mesh was created in Fluent Meshing v23.1 and is shown in Fig. 7. The fluid domain comprised a blend of structured hexahedral cells in the core—away from the boundaries—and unstructured polyhedral cells near the wall for improved boundary layer resolution around the irregular effusion holes. The solid was discretized with exclusively polyhedral cells. It should be noted that the mesh was conformal at the solid-fluid interface and identical between the periodic boundaries. To ensure resolution of the viscous sublayer, a requirement imposed by the selected turbulence model, preliminary calculations were conducted to determine adequate mesh spacing near the wall. Based on the geometry and flow conditions presented, 15 prism layers were used in the near-wall region with a first cell height of 0.002 mm and a transition ratio of 0.272 to achieve $y^+ < 1$.

A mesh independence study was also conducted (Fig. 8) to minimize computational resources while maintaining solution accuracy. Five meshes were generated that ranged from 10.9 to 34.2 million cells. Mesh features deemed to have highest influence on the solution were the length of cells circumnavigating the hole walls, the length of cells in the vicinity of the wall, and the length of cells on the hot- and cold-side surfaces. The average Nusselt number $\overline{Nu}$ on the hot-side wall was used for comparison and is defined as

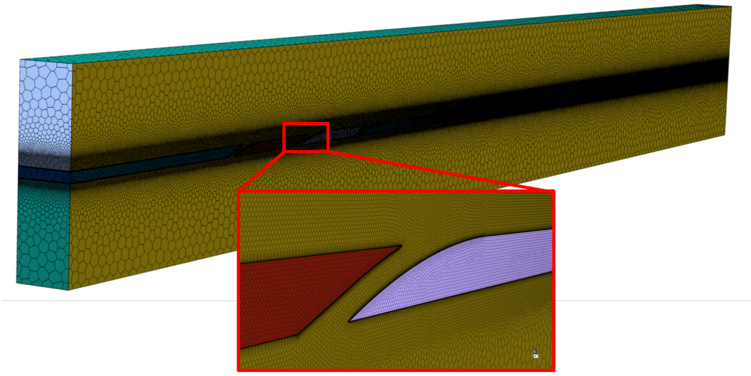

Fig. 7 Mesh for the baseline hole domain with reduced cell size and prism layers near the liner.

$$\overline{Nu} = \frac{\overline{h}L}{\lambda} \tag{4}$$

where $\overline{h}$ is the average hot-side heat transfer coefficient, λ is the fluid thermal conductivity, and L is the characteristic length of the geometry—in this case, the streamwise length from the first hole to the last. The heat transfer coefficient is given as

$$\overline{h} = \frac{\overline{q}}{\overline{T}_w - T_{in,hot}} \tag{5}$$

where $\overline{q}$ and $\overline{T}_w$ are the average hot-side wall heat flux and wall temperature, respectively, and $T_{in,hot}$ is the hot-side inlet temperature. The mesh with approximately 21 million cells was adopted here.

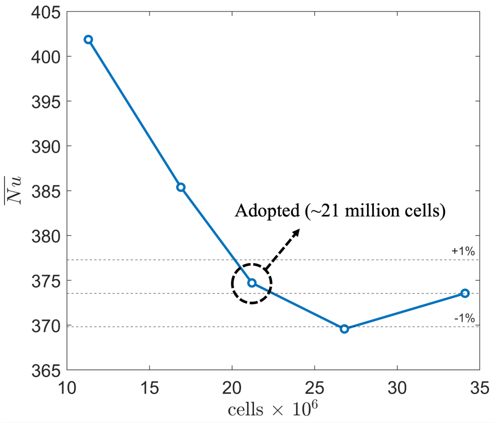

Fig. 8 Mesh independence results at TC2 conditions.

Solution convergence was contingent on the residuals—continuity, x-, y-, and z-velocity, energy, k, and ω—obtaining values lower than 10^{-6}. Additional criteria—temperature T_{pt} and x-velocity u_{pt} at an arbitrary monitor point within the flow, the average hot-side wall heat flux $\overline{q}$, and average hot-side wall temperature $\overline{T}_w$—were observed to further confirm convergence. A threshold of 10^{-4} averaged over 40 iterations was placed on the corresponding residuals. The results (Fig. 9) indicate that the solution met all criteria around 1,500 iterations.

2. Model validation

The computations were compared to the experimental results of Behrendt and Hassa [6] at TC2 conditions. Fig. 10 shows the test sample used in the experiment and the cooling effectiveness η distribution on the hot-side wall within the region indicated by the dotted line. The cooling effectiveness is expressed as

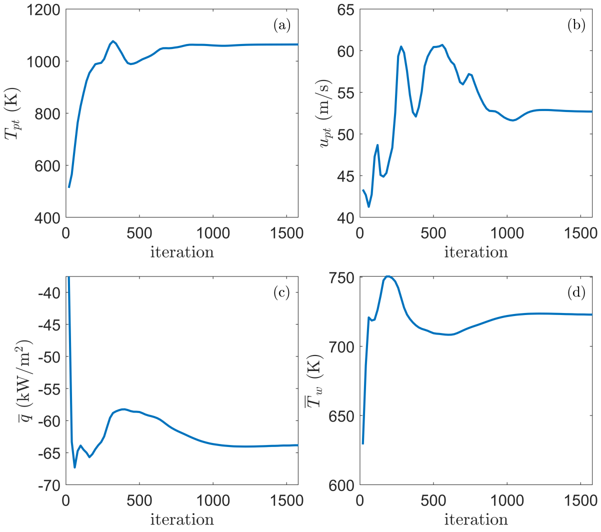

Fig. 9 Convergence of adopted mesh: a) temperature at the monitor point, b) x-velocity at the monitor point, c) average hot-side wall heat flux, and d) average hot-side wall temperature.

$$\eta = \frac{T_{in,hot} - T_w(x, y)}{T_{in,hot} - T_{in,cold}} \tag{6}$$

where $T_{in,hot}$ and $T_{in,cold}$ are the hot- and cold-side inlet temperatures and $T_w(x, y)$ is the local hot-side wall temperature. The surface temperature data was collected using infrared thermography. Further details regarding experimental apparatus and data collection are provided in [6]. Optical access was blocked between $32 \leq x \leq 46$ mm due to the test rig casing, causing the absence of temperature data.

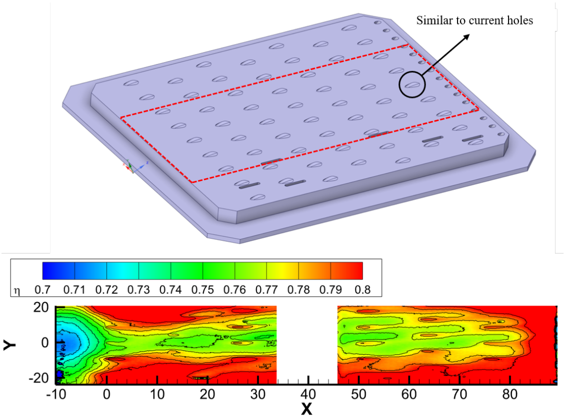

Fig. 10 Test sample used in the Behrendt and Hassa experiment [6] and cooling effectiveness contour (within dotted region) at TC2 conditions.

The simulated grid and test sample share similar streamwise and spanwise hole spacing. The effusion hole shape from the test sample is also similar to that which is presented in Section III.B—sufficiently close for validation purposes. Note, however, that the test sample grid pattern (Fig. 10) repeats only four times in the streamwise direction—the computational grid repeats eight times. As a result, only data from the first four patterns could be compared.

Spanwise cooling effectiveness η_{span} was calculated from the simulation and experiment results and was used as the metric for comparison. Similar to Eq. 6, it is defined as

$$\eta_{span} = \frac{T_{in,hot} - \overline{T}_{w,span}}{T_{in,hot} - T_{in,cold}} \tag{7}$$

where instead of a localized wall temperature $T_w(x, y)$, the spanwise-averaged wall temperature $\overline{T}_{w,span}$ at a given streamwise location is used.

The results are illustrated in Fig. 11. A margin of ±20% relative to the experiment is also provided. Spikes in the simulation data are caused by the presence of a hole at that particular streamwise location; the absence of the wall consequently effects the calculated spanwise-averaged wall temperature.

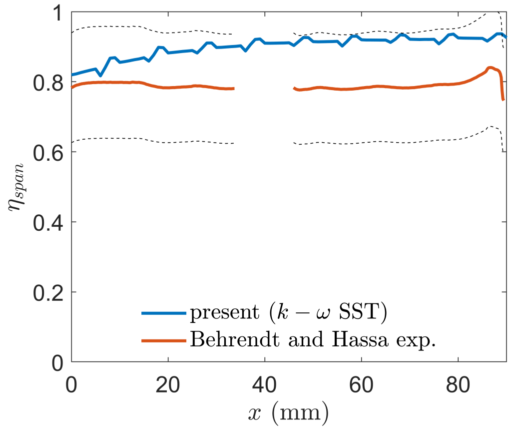

Fig. 11 Spanwise cooling effectiveness for the present model and Behrendt and Hassa experiment [6].

The effectiveness from the experiment remained mostly constant at $\eta_{span} \approx 0.8$. The simulation yielded a similar initial effectiveness, but increased until almost plateauing at $\eta_{span} = 0.91$ around $x = 50$ mm. The difference in trends could be attributed to effects at the boundaries. During an experiment, it is challenging to contain thermal energy within localized areas, ensure uniform velocity and temperature profiles at the inlets, and maintain exact outlet pressures and pressure drops. Of course, these are easily controlled in a numerical setting. Taking these factors into consideration, and realizing the predicted spanwise effectiveness deviates from the experiment by less than 20% throughout the sampled region, the model is considered sufficient for analysis.

To further affirm validity, specifically the use of the $k-\omega$ SST turbulence model, the exact geometry and flow conditions presented in a series of papers [7–9]—large eddy simulations (LES) of combustor effusion holes with conjugate heat transfer—were recreated here. The solution domain and boundary conditions are presented in Fig. 12. The operating conditions are provided in Table 4 and are notably similar in magnitude to those of TC2. Details of the hole geometry and grid spacing are provided in the original papers.

Table 4 Operating conditions from Refs. [7–9].

Parameter	Hot path	Cold path
T_{in} (K)	1600	600
P_{out} (bar)	4.5	4.725 ($\Delta P = 5\%$)
u_{in} (m/s)	25	50

Similar to Fig. 11, a comparison of spanwise cooling effectiveness is shown in Fig. 13. The ±20% experimental error margin is indicated by the dotted lines. The $k-\omega$ SST model adequately replicates the trends observed by the LES model within an acceptable limit. Fig. 14(a)-(b) shows, respectively, the development of spanwise-averaged mass flux and temperature profiles near the wall at four streamwise locations along the grid. The vertical distance from the wall y^* was taken as the physical distance normalized by the stramwise grid spacing—details are provided in [8]. The present results with the $k-\omega$ SST model demonstrate comparable near-wall flow and thermal development relative to the LES throughout the solution domain. Thus, the implemented numerical methods and turbulence model are again verified.

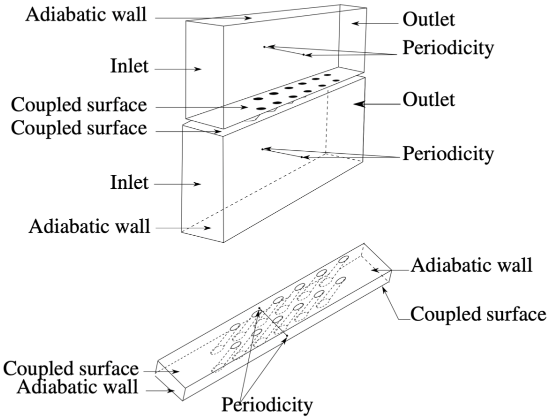

Fig. 12 Geometry and boundary conditions used in Refs. [7–9].

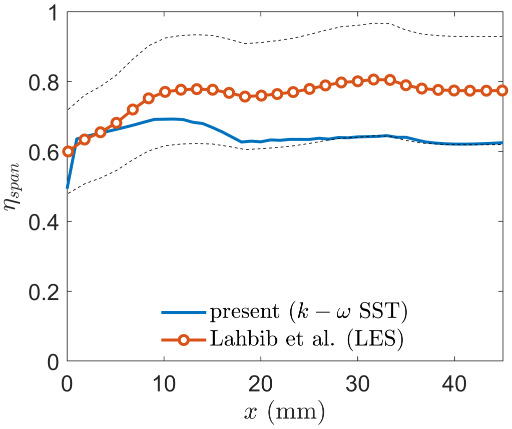

Fig. 13 Spanwise cooling effectiveness using RANS with $k-\omega$ SST (present) compared to LES [7].

IV. Results

A. Inlet fillet

Fig. 15 displays the spanwise cooling effectiveness for the baseline and variations v1 and v2, whose inlets were filleted at the trailing edge (Fig. 5). As mentioned previously, the spikes result from the presence of the holes. Unlike Fig. 11, which illustrates the baseline results for only the first four grid patterns (see Section III.D.2), the baseline results of the entire grid (all 8 streamwise patterns) is shown here. For all three cases, the effectiveness quickly increased from η_{span} = 0.82 to 0.91 at $x \approx 50$ mm, from which point it maintained a gradual yet subtle upward trend to η_{span} 0.93.

Unsurprisingly, the inlet fillet had marginal influence on the hot-side wall characteristics, at least in terms of temperature distribution. This is further exemplified by Fig. 16, which provides a contour of the local cooling effectiveness over the entire grid. The uniform spanwise effectiveness (temperature) at a particular streamwise location indicates that a well-distributed film coverage was achieved from the expansion at the hole outlet. The rapid rate at which the wall initially cools and reaches a uniform temperature is directly influenced by the evenly distributed film.

Fig. 17 shows contours of x-velocity for the baseline and inlet variations v1 and v2 at the fourth hole (from the left) along the grid centerline. From inspection, it is clear that the inlet fillet influences the flow distribution—at least within the hole—compared to the baseline. The differences between the two fillet diameters (v1 and v2) are negligible. The fillets raised the bulk streamwise velocity in the hole. This slightly increased jet velocity at the hole outlet, resulting in better jet attachment along the hot-side wall. However, this higher exit velocity obviously had minimal, if any, effect on the cooling effectiveness since the geometry of the hole outlet already provided sufficient film coverage.

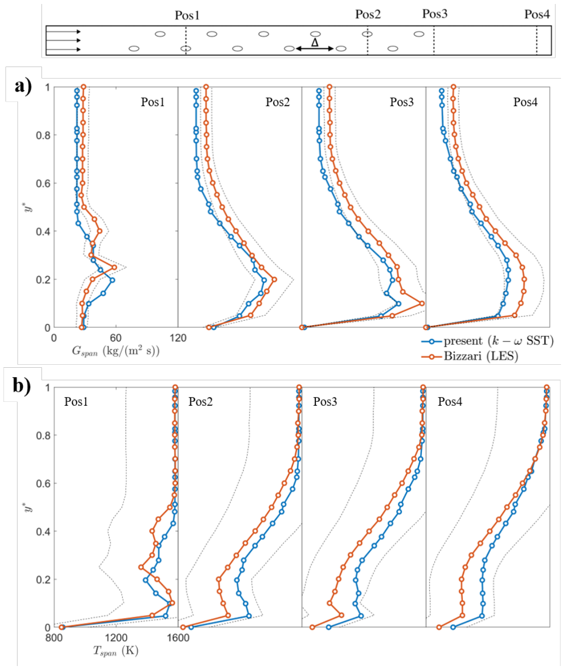

Fig. 14 Development of a) mass flux and b) temperature profiles near the wall using RANS with $k-\omega$ SST (present) compared with LES [8].

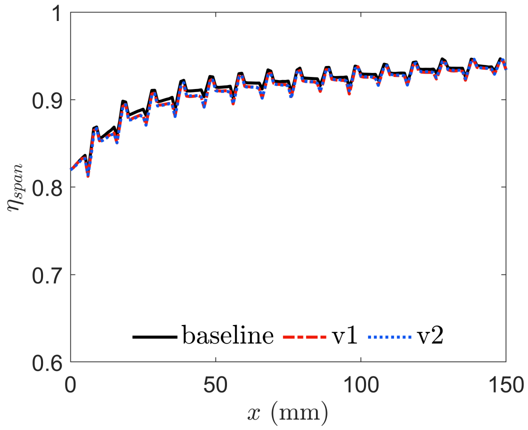

Fig. 15 Spanwise cooling effectiveness for the baseline compared to variations v1 and v2.

B. Width expansion

Fig. 18 again shows spanwise cooling effectiveness of the baseline, but now compared to variations v3 - v5 with different width expansion characteristics (see Fig. 6). Unlike the baseline, v3 and v4 experienced a drop in cooling effectiveness through $x \approx 50$ mm, while v5 remained mostly constant in this region. The effectiveness then steadily increased through the rest of the grid for all three variations. The rate at which the effectiveness increased corresponds to the hole outlet expansion; the wall cooled faster in the presence of a larger outlet (v5) relative to a thinner outlet (v3). The regions of poor effectiveness—especially for v3 and v4—are better illustrated in Fig. 19 between the third and fifth holes (from the left, along the grid centerline). Unlike the variations, all of which had a relatively narrow injection shape, the baseline holes expanded to allow continuous and fast-developing spanwise film protection.

Fig. 20 shows the surface heat flux distributions. Here, a negative heat flux (darker shade) indicates heating the solid, while a positive heat flux (lighter shade) represents cooling. The baseline—which has the largest expansion—has the most distributed spanwise cooling heat flux. For this configuration, the localized negative heat flux (i.e. heated)

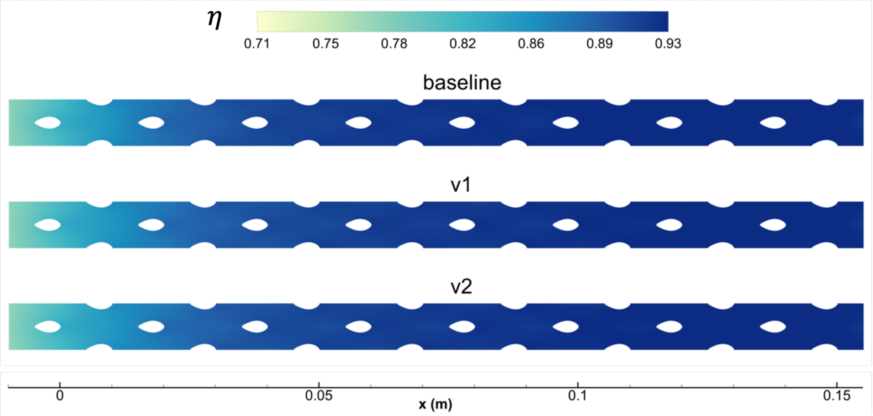

Fig. 16 Cooling effectiveness contours for the baseline and variations v1 and v2.

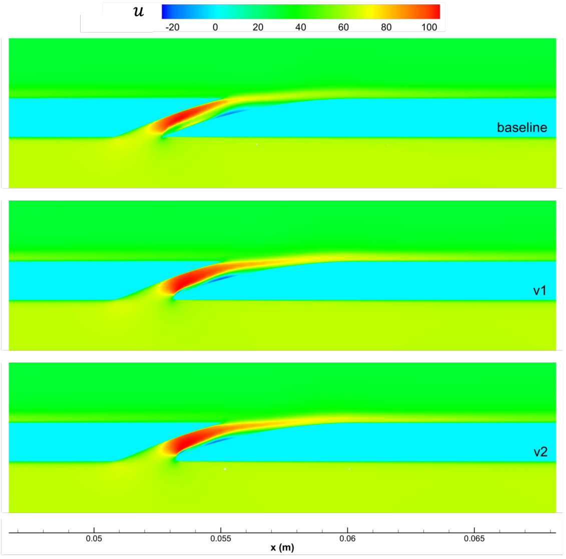

Fig. 17 x-velocity contours for the baseline and variations v1 and v2, located at the fourth hole along the grid centerline.

regions behind each hole imply that the outlet shape may be slightly over-expanded for the specific conditions tested here. For variations v3 - v5, it is not only clear that the regions of cooling heat flux are directly aligned with the focused streamwise jets, but also that the intensity of the cooling streaks increases with increasing outlet shape. The latter point aligns with the findings of Fig. 18.

The more intensely heated regions of v3 - v5 (Fig. 20) between the third and fifth centerline holes naturally corresponded to a lower effectiveness (Fig. 19). The wall heat flux phenomena can be described through inspection of the flow profile above the surface; this is shown in Fig. 21. Here, a frontal (streamwise) view of the fourth centerline hole is shown with x-velocity contours and in-plane velocity vectors, whose components are in the z- and y-directions.

The areas of undesirable heating—especially for v3 and v4—was caused by pairs of counter-rotating vortices circulating hot air from the main flow towards the wall. For the first few grid patterns, the circulation increased the surface temperature (Fig. 19) before a protective film could develop. Even after the development of its cooling film, the unfavorable vortices and relatively focused jets of v3 hindered the ability to increase the effectiveness above the initial state (Fig. 18).

The outlet expansion of v5 was large enough to impair its vortex structures (Fig. 21), but not too large to prevent adverse affects on the wall altogether. Conversely, the vortices in the baseline case rotated opposite those of v3 and v4 due to the wider expansion. These vortices actually convected hot air away from the surface which enhanced inter-row

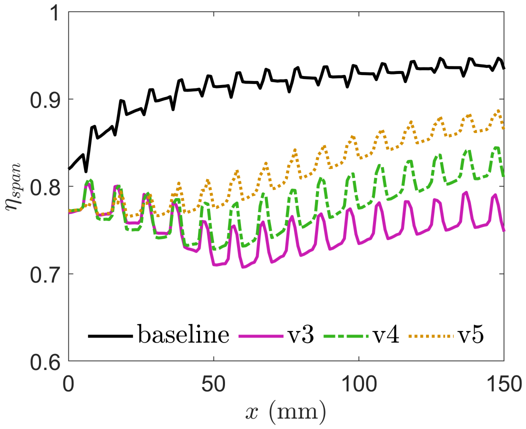

Fig. 18 Spanwise cooling effectiveness for the baseline compared to variations v3 - v5

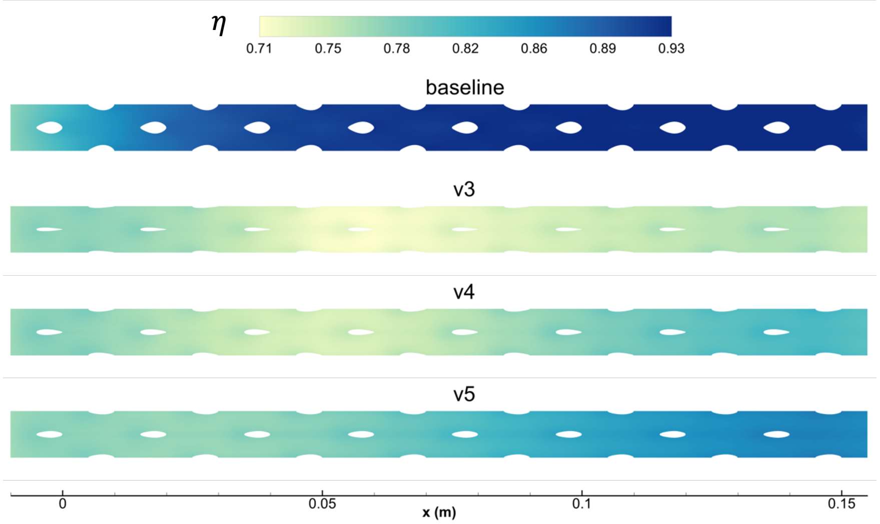

Fig. 19 Cooling effectiveness contours for the baseline and variations v3 - v5.

cooling (Fig. 20), at least in close proximity to each hole's exit.

The characteristics of the vortices are of course influenced by the streamwise momentum of the jet. Fig. 22 illustrates, for each case, an x-velocity contour along the grid centerline and spanning between the the third and fifth holes. The thin injection shapes of v3 and v4 promoted higher streamwise velocity out of the exit, causing the jet to detach from the surface (i.e. jet lift-off). The vertical component of the lift-off and its high velocity—relative to the main flow—induced the counter-rotating vortices away from the jet. Such flow structures can reduce the stability of the film, making it more susceptible to potential disturbances in the main flow. The lift-off seen in v3 and v4 is also responsible for the low-intensity in-line cooling streaks (Fig. 20).

For the baseline, the over-expansion reduced jet momentum at the hole exit and consequently prevented jet lift-off (Fig. 22). However, this caused insufficient streamwise cooling coverage (Fig. 20). The jets from the baseline holes clearly lacked enough momentum to reach the immediate downstream hole. A reduced expansion or higher porosity may yield a more even streamwise heat flux. However, the higher heat flux regions for the baseline case seem to marginally impact the cooling effectiveness in the corresponding regions (Fig. 19), which is ultimately of most significance.

The temperature contours shown in Fig. 23 reiterate the trends introduced by Figs. 19-22. Higher lift-off reduced the film coverage and thus lowered cooling effectiveness. For v3 - v5, the temperature of the solid is noticeably hotter than that in the baseline configuration. Although a 2D cross-section is shown, it can be inferred that the warmer air trapped under the film in v3 was caused by the vortices (discussed previously) circulating hot flow towards the wall. The

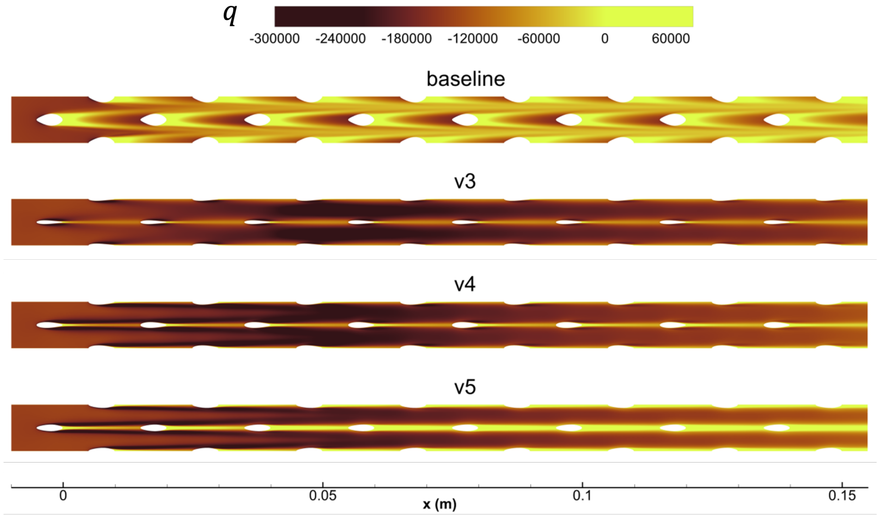

Fig. 20 Heat flux contours for the baseline and variations v3 - v5.

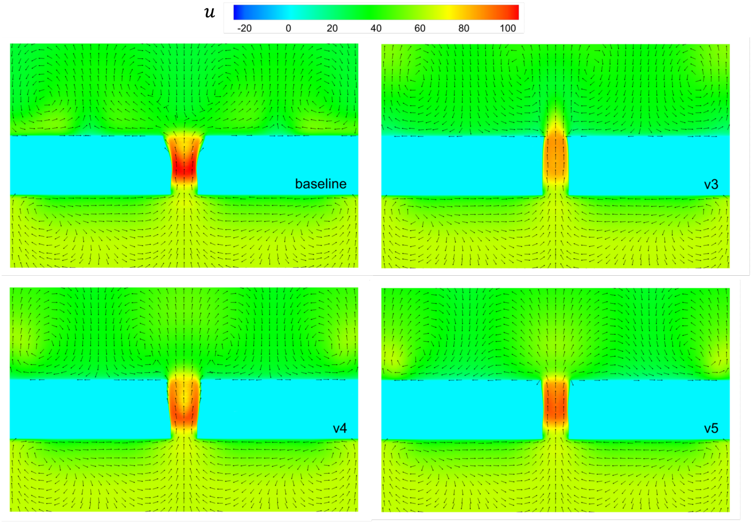

Fig. 21 Frontal (streamwise) view of x-velocity contours of the fourth centerline hole, shown for the baseline and v3 - v5.

consistent temperature profile shown in the baseline case also suggests that, while the heat flux may be uneven down the centerline due to over-expansion (Fig. 20), the neighboring holes provide adequate coverage up to the next downstream hole.

V. Conclusions

Simulations were conducted to investigate the cooling performance of a novel fuel-lean combustor effusion hole under realistic operating conditions. The shape of the hole was derived from a quadratic Bézier curve, with the aim of injecting cooling air to the liner more effectively than traditional effusion geometries. The baseline hole configuration was altered to observe the effects of an inlet fillet and the expansion width of the channel. Unique hole shapes such as those introduced here are enabled in practice by recent developments in additive manufacturing practices.

The results indicate that the inlet fillet both increased the streamwise velocity within the hole and (slightly) improved flow attachment, but overall had minimal effect on the hot-side liner characteristics. With respect to width expansion, the baseline geometry yielded the highest cooling effectiveness and most even surface heat flux distribution. Thinner

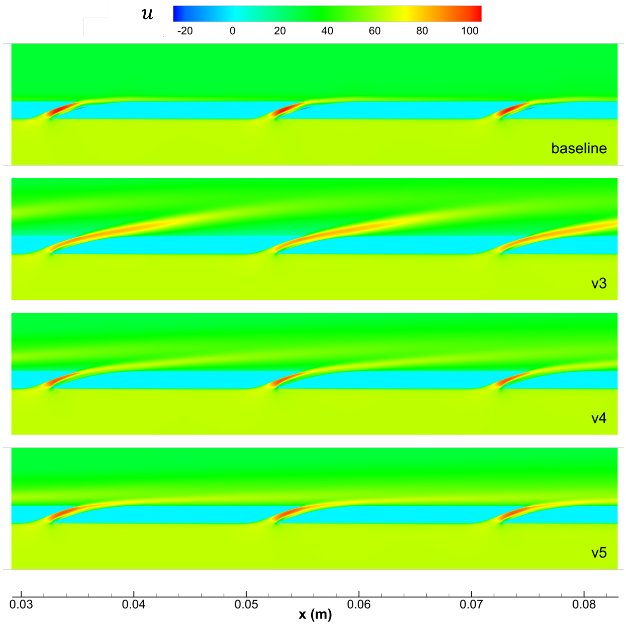

Fig. 22 x**-velocity contours for the baseline and variations v3 - v5, between the third and fifth holes along the grid centerline.**

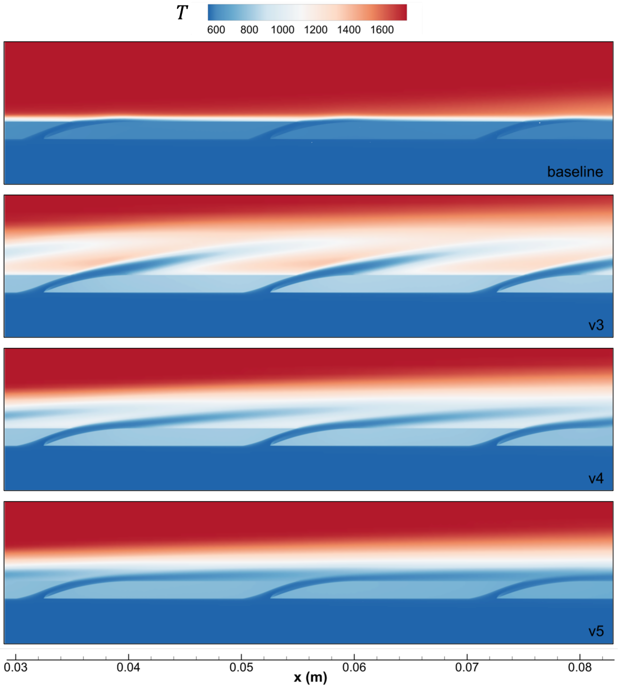

Fig. 23 Temperature contours for the baseline and variations v3 - v5, between the third and fifth holes along the grid centerline.

injection-side holes increased the jet momentum, causing lift-off and localized heated regions resulting from unfavorable vortex structures. Further simulations will be carried out to enhance the configuration and investigate factors such as higher pressure gradients, radiation, and transient conditions.

Acknowledgments

The authors express their gratitude to Embry-Riddle Aeronautical University and the Deutsches Zentrum für Luft- und Raumfahrt (DLR) for providing the computational resources and facilities required to complete this research. This material is based upon work supported by the National Science Foundation grant no. OISE 1460045.

References

[1] Teoh, L. E., and Khoo, H. L., "Green air transport system: An overview of issues, strategies and challenges," *KSCE Journal of Civil Engineering*, Vol. 20, No. 3, 2016, pp. 1040–1052. https://doi.org/10.1007/s12205-016-1670-3.

[2] Schulz, A., "Combustor Liner Cooling Technology in Scope of Reduced Pollutant Formation and Rising Thermal Efficiencies," *Annals of the New York Academy of Sciences*, Vol. 934, No. 1, 2001, pp. 135–146. https://doi.org/10.1111/j.1749-6632.2001.tb05848.x.

[3] Ranasinghe, K., Guan, K., Gardi, A., and Sabatini, R., "Review of advanced low-emission technologies for sustainable aviation," *Energy*, Vol. 188, 2019, p. 115945. https://doi.org/10.1016/j.energy.2019.115945.

[4] Afonso, F., Sohst, M., Diogo, C. M., Rodrigues, S. S., Ferreira, A., Ribeiro, I., Marques, R., Rego, F. F., Sohouli, A., Portugal-Pereira, J., Policarpo, H., Soares, B., Ferreira, B., Fernandes, E. C., Lau, F., and Suleman, A., "Strategies towards a more sustainable aviation: A systematic review," *Progress in Aerospace Sciences*, Vol. 137, 2023, p. 100878. https://doi.org/10.1016/j.paerosci.2022.100878.

[5] Motheau, E., Lederlin, T., Florenciano, J. L., and Bruel, P., "LES Investigation of the Flow Through an Effusion-Cooled Aeronautical Combustor Model," *Flow, Turbulence and Combustion*, Vol. 88, No. 1–2, 2011, pp. 169–189. https://doi.org/10.1007/s10494-011-9357-9.

[6] Behrendt, T., and Hassa, C., "A test rig for investigations of gas turbine combustor cooling concepts under realistic operating conditions," *Proceedings of the Institution of Mechanical Engineers, Part G: Journal of Aerospace Engineering*, Vol. 222, No. 2, 2008, pp. 169–177. https://doi.org/10.1243/09544100jaero288.

[7] Lahbib, D., Dauptain, A., Duchaine, F., and Nicoud, F., "Large Eddy Simulation of Conjugate Heat Transfer Around a Multi-Perforated Plate With Deviation," *Volume 5A: Heat Transfer*, American Society of Mechanical Engineers, 2016. https://doi.org/10.1115/gt2016-56442.

[8] Bizzari, R., "Aerodynamic and thermal modelling of effusion cooling in LES," Ph.D. thesis, 11 2018.

[9] Bizzari, R., Lahbib, D., Dauptain, A., Duchaine, F., Gicquel, L. Y. M., and Nicoud, F., "A Thickened-Hole Model for Large Eddy Simulations over Multiperforated Liners," *Flow, Turbulence and Combustion*, Vol. 101, No. 3, 2018, pp. 705–717. https://doi.org/10.1007/s10494-018-9909-3.

[10] Agazhanov, A. S., Samoshkin, D. A., and Kozlovskii, Y. M., "Thermophysical properties of Inconel 718 alloy," *Journal of Physics: Conference Series*, Vol. 1382, No. 1, 2019, p. 012175. https://doi.org/10.1088/1742-6596/1382/1/012175.

[11] Zuckerman, N., and Lior, N., "Impingement Heat Transfer: Correlations and Numerical Modeling," *Journal of Heat Transfer*, Vol. 127, No. 5, 2005, pp. 544–552. https://doi.org/10.1115/1.1861921.

[12] Jackowski, T., Elfner, M., and Bauer, H.-J., "Numerical Investigation of Conjugate Heat Transfer in an Effusion and Impingement Cooled Combustor Wall," *Volume 7A: Heat Transfer*, American Society of Mechanical Engineers, 2020. https://doi.org/10.1115/gt2020-15505.

[13] Lu, X., Jia, Y., Ji, Y., Ge, B., and Zang, S., "Effect of the hole configurations on effusion cooling effectiveness under swirl impact in gas turbine combustor," *International Journal of Thermal Sciences*, Vol. 203, 2024, p. 109164. https://doi.org/10.1016/j.ijthermalsci.2024.109164.